



Genetic identification and fisher identifiability analysis of the Doyle–Fuller–Newman model from experimental cycling of a LiFePO₄ cell

Joel C. Forman^a, Scott J. Moura^b, Jeffrey L. Stein^a, Hosam K. Fathy^{c,*}

^a The University of Michigan, Ann Arbor, MI 48109, USA

^b University of California San Diego, San Diego, CA 92093, USA

^c The Pennsylvania State University, University Park, PA 16802, USA

ARTICLE INFO

Article history:

Received 23 December 2011

Received in revised form 4 March 2012

Accepted 6 March 2012

Available online 29 March 2012

Keywords:

Parameter identification

Electrochemical battery modeling

Li-ion batteries

Genetic algorithms

Fisher information

ABSTRACT

This article examines the problem of identifying the physical parameters of fundamental electrochemistry-based battery models from non-invasive voltage/current cycling tests. The article is particularly motivated by the problem of fitting the Doyle–Fuller–Newman (DFN) battery model to lithium-ion battery cycling data. Previous research in the literature identifies subsets of the DFN model's parameter experimentally. In contrast, this article makes the two unique contributions of: (i) identifying the full set of DFN model parameters from cycling data using a genetic algorithm (GA), and (ii) assessing the accuracy and identifiability of the resulting full parameter set using Fisher information. The specific battery used within this study has lithium iron phosphate cathode chemistry and is intended for high-power applications such as plug-in hybrid electric vehicles (PHEVs). We use seven experimental cycling data sets for model fitting and validation, six of them derived from PHEV drive cycles. This makes the identified parameter values appropriate for PHEV battery simulation and model-based design and control optimization.

© 2012 Elsevier B.V. All rights reserved.

1. Introduction

This article examines the problem of identifying the parameters of the electrochemical battery model developed by Doyle, Fuller, and Newman (DFN) [1,2] using noninvasive voltage–current cycling experiments. The article presents a framework for solving this problem, consisting of a genetic algorithm (GA) for parameter identification combined with Fisher information-based estimation of parameter identifiability and identification errors. We apply this framework to LiFePO₄ battery cells intended for plug-in hybrid electric vehicles (PHEVs). The ultimate goal is to obtain an experimentally validated, electrochemistry-based model of these batteries that can enable the optimization of PHEV design and control for objectives such as reducing PHEV fuel consumption and greenhouse gas emissions [3].

The DFN model is well-suited for this study because it is a first-principles electrochemical model that can capture high-rate transient effects. In contrast to equivalent circuit models, first-principles models make it easier to relate model parameters back to physical quantities (such as diffusivity and porosity). This is

important because one of our goals is to investigate the accuracy with which one can estimate these physical quantities from non-invasive voltage and current data. The DFN model also captures high-rate transient effects typical of PHEV applications. In particular, a recent study by Santhanagopalan et al. shows that the DFN model fits battery behavior above 1C current rates better than a single particle model (SPM) [4]. The DFN model achieves these advantages over the SPM in part by modeling spatial distributions of lithium across the width of the anode, separator, and cathode. These effects are ignored in SPMs.

A significant body of literature already exists on battery parameter identification using different models and identification methods for different parameter sets. Here we focus exclusively on identification methods that, like our own work, are intended for offline use. Santhanagopalan et al., for instance, successfully identify a subset of five parameter values under constant charge and discharge conditions for both the DFN and SPM models [4]. In both cases, the Levenberg–Marquardt optimization algorithm is used to obtain parameters that minimize model error. Speltino et al. successfully identify the parameters of a single-particle model of battery dynamics using a two-step process: they first identify the cathode equilibrium potential function from open circuit voltage measurements, assuming a known anode equilibrium potential function from the literature. They subsequently perform dynamic tests to estimate the remaining model parameters [5]. Schmidt et al. also

* Corresponding author. Tel.: +1 814 867 4442; fax: +1 814 865 7222.

E-mail addresses: jcforman@umich.edu (J.C. Forman), smoura@ucsd.edu (S.J. Moura), stein@umich.edu (J.L. Stein), hkf2@psu.edu (H.K. Fathy).

successfully identify a single-particle battery model, with several extensions that incorporate temperature information and relate solid diffusion to state of charge [6]. The study by Schmidt et al. also examines parameter uncertainty using Fisher information. Finally, Hu et al. successfully identify the parameters of an equivalent circuit battery model using a genetic algorithm [7]. They focus on two types of batteries, one of which is the A123 Systems 26650 cell examined in this article. Their equivalent circuit formulation is a set of n parallel resistor–capacitor pairs connected to each other in series.

The above literature provides a rich background for this article. In contrast to that background, this work achieves a combination of five important goals never pursued simultaneously in the previous literature – to the best of the authors' knowledge. First, we focus on identifying parameters of the DFN model: a choice justified by this model's first-principles nature and suitability for high-rate transient battery operation. Second, we identify the full set of parameters (88 scalars and function control points) of the DFN model using a genetic algorithm, as opposed to a subset of these parameters. Third, we perform this identification using multiple battery cycles derived from vehicle drive cycles. (Note, altogether, these three choices of battery model, identification parameters, and cycling data represent an overarching goal of obtaining a DFN parameter set suitable for PHEV simulation and design/control optimization.) Fourth, we use Fisher information to assess the accuracy of all 88 DFN model parameters, as opposed to computing Fisher information for a subset of these parameters. This is extremely important, because a parameter deemed identifiable based on Fisher information computation for a small parameter set may lose identifiability when one computes Fisher information for a larger parameter set. Finally, we qualitatively correlate the Fisher information-based identifiability results to physical insights about the dominant dynamics in the LiFePO₄ battery for the test conditions examined herein. These two final contributions distinguish this article from an earlier paper by the authors that qualitatively investigated DFN parameter uncertainty using the identifiability matrix [8]. Results in this earlier paper suggest that while the DFN model can fit battery cycling data well, certain parameters remain unidentifiable. This article enhances these results by quantifying parameter uncertainty via Fisher information. Fisher information provides a minimum variance bound for the estimated parameters via the Cramér–Rao inequality [9–13]. In addition, this article provides original insights about the dominant dynamics in the LiFePO₄ battery under the tests considered herein, and relates these insights to parameter uncertainties.

The remainder of this article is organized as follows. Section 2 describes the experiments used for identifying the DFN model. This includes a discussion of the experimental setup along with the various PHEV drive cycle inputs. Section 3 summarizes the DFN model. Sections 4 and 5 describe the unknown parameter set and genetic optimization algorithm, respectively. Section 5 also briefly describes model reduction methods used to simulate the DFN model, including quasi-linearization and modal decomposition [14,15]. Section 6 presents validation studies for the identified model. This includes voltage and power trajectories of validation data along with probability density plots summarizing the errors. Finally, Section 7 presents the Fisher information results on parameter accuracy analysis along with conjectures about dominant dynamics based on parameter uncertainty. Section 8 summarizes and concludes the paper.

2. Experimental setup

The battery cells examined in this article are A123 Systems ANR26650M1 cells with LiFePO₄ cathodes. These cells have a

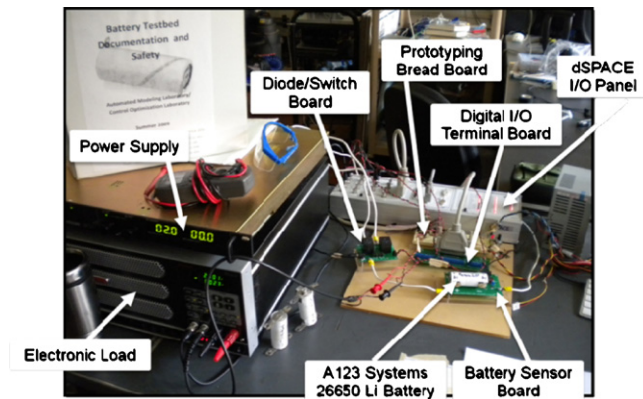


Fig. 1. Photograph of experimental battery tester.

2.3A-h nominal capacity when fresh, a nominal voltage of 3.3 V, and a maximum continuous discharge current of 70 A (30.4 C-rate). The cells are intended for transient high-power applications including commercial PHEVs, PHEV conversion kits, and portable power tools. Experimental cycling data sets have been collected for these cells using a custom-built battery tester. This tester is capable of highly transient current/voltage profiles and can switch quickly between charging and discharging. These characteristics make it ideal for testing batteries under conditions similar to those experienced in PHEV battery packs. Additionally, this setup is capable of battery-in-the-loop studies, which will be advantageous for future battery control and estimation research [16].

The above battery tester combines three major hardware components: an electric load (Sorenson SLH-60-120-1200), a power supply (Sorenson DSC20-50E), and a Real-Time (RT) controller and I/O board (dSpace DS1104). Fig. 1 is a photograph of the battery tester, and Fig. 2 is a schematic of the setup where all signal lines are connected to the I/O board. The power supply and electric load handle battery charging and discharging, respectively. The RT I/O board coordinates the electric load, power supply, and switching board. In addition, the RT I/O board records sensor signals including voltage and current. These signals are exchanged among the setup's various components in a variety of formats, including the analog, digital, PWM, SMBus, RS-232, and TTL formats. The switch board swaps the setup between charging and discharging by swapping the battery's connection between the power supply and load. The Schottky diode protects the power supply from absorbing battery energy. The battery sensor board measures battery voltage through a voltage-isolating differential op-amp, and measures battery current via a bi-directional ± 20 A Hall effect sensor (Allegro Microsystems ACS714). Finally, all the battery interface electronics are implemented on custom-build Printed Circuit Boards (PCBs) to maximize overall setup reliability, which is critical for long-term tests.

Seven battery cycling tests have been conducted using this battery tester: two for model identification and five for validation. All of these tests initialize the battery SoC to 90% (3.35 V relaxed), then subject the battery to a given current profile and measure the resulting battery voltage. In the first identification data set, the current profile consists of a *Chirp* sequence of three CCCV charge/discharge patterns between 2.0 V and 3.6 V, with charge/discharge rates of 5 C, 2.5 C, and 1 C. In the remaining tests, the current profiles are generated by simulating a PHEV powertrain for a given vehicle drive cycle (i.e., velocity-versus-time profile). Two of these vehicle drive cycles correspond to the morning and evening commutes of a real human driver in a naturalistic driving study conducted by the University of Michigan Transportation Research Institute (UMTRI) [17]. These drive cycles are exact

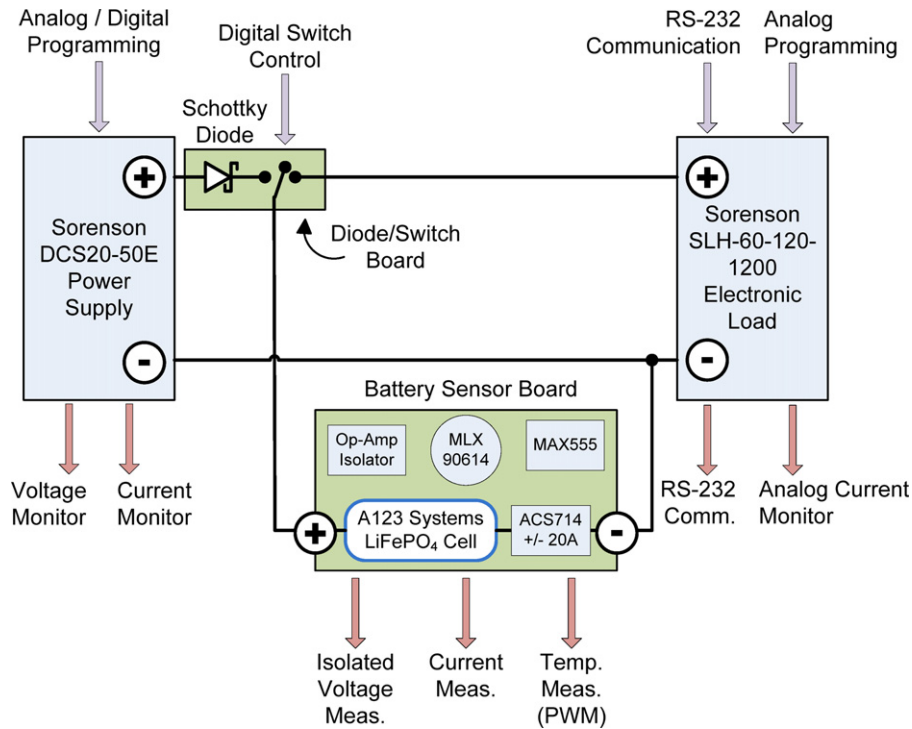


Fig. 2. Schematic of experimental battery tester.

recordings of driver behavior using mid-sized sedans, these two specific cycles correspond to the same sedan on the same day. These battery tests are denoted as *Naturalistic1* and *Naturalistic2*, respectively. The four remaining battery tests correspond to multiple repetitions of standard vehicle certification drive cycles. These battery tests are denoted by *UDDSx2*, *US06x3*, *SC03x4*, and *LA92x2*, where the number in “x#” refers to the number of drive cycle repetitions [18]. For each of these drive cycle-based battery tests, a mid-size power-split sedan PHEV is simulated with a previously optimized power management algorithm [19] to map the vehicle drive cycles to battery current profiles. This PHEV has a 5 kWh battery pack consistent with existing Toyota Prius PHEV conversion kits. Due to sensor limitations, drive cycles that produce current magnitudes greater than 20 A (namely, *US06x3*, *SC03x2*, and *LA92x2*) are scaled down such that their maximum amplitude over time is 20 A [18]. Specifically, this scaling divides the current trajectory by its maximum current and then multiplies the trajectory by 20. Finally, the resulting current profiles are applied to the battery cell to obtain data sets for identification and validation.

3. The Doyle–Fuller–Newman battery model

The DFN model is an electrochemical battery model that describes the dynamics of concentration and potential distributions across the width of the cell as well as concentration profiles in the porous electrodes of the anode and cathode. Spatial distributions across the width of the cell play an important role in high-rate charge and discharge dynamics, typical of PHEV cycles. The model is described thoroughly in [1,2,20]. This section summarizes the model equations, which constitute a nonlinear partial differential algebraic equation system. Appendix contains the model's boundary conditions.

As seen in Fig. 3, a Li-ion battery cell consists of an anode, separator, and cathode sandwiched between current collectors. Both the anode and cathode are made of porous solid material immersed in an electrolyte solution. When the battery is fully charged, lithium ions occupy interstitial sites in the anode-side solid material. As the

battery discharges, the Li-ions leave these interstitial sites, entering the electrolyte solution. The Li-ions then migrate through the solution from the anode to the separator, and eventually the cathode. The discharging process concludes with the lithium ions coming to rest at interstitial sites in the cathode-side solid material. When a Li-ion leaves its interstitial site in the anode an electron is freed to flow through the external circuit, producing useful work. When this electron reaches the cathode it causes a Li-ion to bond with a cathode interstitial site. Charging the battery is the same process in reverse, with the external circuit providing rather than consuming energy.

The DFN model captures local Li-ion concentrations and potentials using coupled partial differential equations (PDEs). These PDEs account for the linear diffusion of Li-ions in the electrolyte,

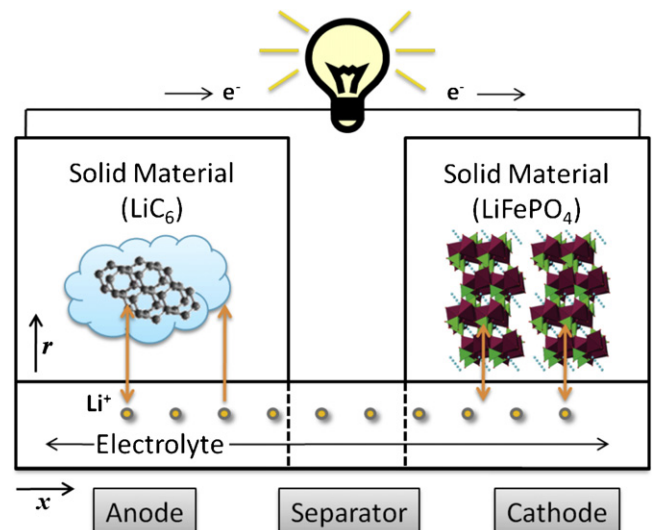


Fig. 3. Li-ion cell schematic.

Table 1
Unknown parameters.

Name	Unit	Description
L_n	m	Anode thickness
L_s	m	Separator thickness
L_p	m	Cathode thickness
R_n	m	Anode particle radius
R_p	m	Cathode particle radius
t^+	–	Transference number
b	–	Brugman number
d_2	$\text{m}^2 \text{s}^{-1}$	Solution diffusivity
ε_{2n}	–	Anode solution volume fraction
ε_{2s}	–	Separator solution volume fraction
ε_{2p}	–	Cathode solution volume fraction
d_{1n}	$\text{m}^2 \text{s}^{-1}$	Anode solid diffusivity
d_{1p}	$\text{m}^2 \text{s}^{-1}$	Cathode solid diffusivity
k_n	$(\text{A m}^{-2})(\text{mol m}^{-3})^{1+\alpha}$	Anode reaction rate
k_p	$(\text{A m}^{-2})(\text{mol m}^{-3})^{1+\alpha}$	Cathode reaction rate
R_{SEI}	$\Omega \text{ m}^2$	Anode film thickness
c_2	mol m^{-3}	Initial solution concentration
u_{nref}^i	V	Anode equilibrium potential function: control point i
u_{pref}^i	V	Cathode equilibrium potential function: control point i
κ_i	$\Omega^{-1} \text{ m}^{-1}$	Solution conductivity function: control point i

spherical diffusion of Li-ions in the solid, and the spatially distributed electrochemical reactions driving them to transfer between the solution and the solid. The remainder of this section briefly outlines these equations. The parameters of these equations are summarized in Table 1 and all of the boundary conditions for these equations are summarized in Appendix.

The concentration of Li-ions within the electrolyte $c_2(x, t)$ is governed by Fick's law of linear diffusion combined with an intercalation current density term, J , transferring Li-ions between the solution and solid:

$$\varepsilon_2 \frac{\partial c_2}{\partial t}(x, t) = \frac{\partial}{\partial x} \left(d_2^{\text{eff}} \frac{\partial c_2}{\partial t}(x, t) \right) + \frac{1-t^+}{F} J(x, t) \quad (1)$$

The above intercalation reaction current density, J , also acts as an input to the dynamics of Li-ion diffusion within the solid. This diffusion occurs at every point in the anode and cathode and can be modeled using a spherical, radially symmetric diffusion law as follows:

$$\frac{\partial c_{1,j}}{\partial t}(r, t) = \frac{d_{1,j}}{r^2} \frac{\partial}{\partial r} \left(r^2 \frac{\partial c_{1,j}}{\partial r}(r, t) \right) \quad (2)$$

where we note that while radial spherical diffusion is an appropriate model for the anode, it is only an approximation for the cathode. We refer the interested reader to papers on both understanding the behavior of the LiFePO₄ cathode [21–23] and agglomerate type models that capture various aspects of the electrode's behavior [24–29].

The intercalation reaction current density, J , is driven by potential differences between the solid and electrolyte solution, as governed by the Butler–Volmer equation:

$$J(x, t) = a_j i_{0,j} \left[\exp \left(\frac{\alpha_{a,j} F}{RT} \eta_j(x, t) \right) - \exp \left(-\frac{\alpha_{c,j} F}{RT} \eta_j(x, t) \right) \right] \quad (3)$$

$$i_{0,j} = k_j (c_{1,j}^{\text{max}} - c_{1,j}^S)^{\alpha_{a,j}} (c_{1,j}^S)^{\alpha_{c,j}} (c_2)^{\alpha_{a,j}}, \quad j = n, p \quad (4)$$

The overpotentials in the above equations, η_j , equal the differences between the solid and solution potentials minus the reference potentials for the main intercalation reaction, which in

turn depend on the local states of charge. Mathematically the overpotentials are given by:

$$\eta_p(x, t) = \phi_1(x, t) - \phi_2(x, t) - u_{pref}(x, t) \quad (5)$$

$$\eta_n(x, t) = \phi_1(x, t) - \phi_2(x, t) - u_{nref}(x, t) - \frac{J(x, t)}{a_n} R_{SEI} \quad (6)$$

Since potentials and overpotentials described above have dynamics orders of magnitude faster than the Li-ion concentrations, they are assumed to respond instantaneously. The solid potential is governed by Ohm's law with a source term governing the charge transfer due to intercalation:

$$\frac{\partial}{\partial x} \left(\sigma_j^{\text{eff}} \frac{\partial \phi_{1,j}}{\partial x}(x, t) \right) - J(x, t) = 0 \quad (7)$$

Similarly, the solution potential is governed by Ohm's law, intercalation current density, and the charge carried by the ions in solution:

$$\frac{\partial}{\partial x} \left(\kappa^{\text{eff}} \frac{\partial \phi_2}{\partial x}(x, t) \right) + J(x, t) + \frac{\partial}{\partial x} \left(\kappa_D \frac{\partial}{\partial x} \ln(c_2(x, t)) \right) = 0 \quad (8)$$

The above system of equations are the DFN model that represent the dynamics of charging and discharging in the Li-ion cell. The boundary conditions for this model are given in Appendix. When the DFN model is discretized it becomes a system of Differential Algebraic Equations (DAEs), where the differential equations govern the diffusion dynamics and the algebraic equations constrain the potentials and intercalation current accordingly.

4. Parameter set

This section describes the DFN model parameters identified in this paper, and explains some of the constraints placed on these parameters during identification. The parameters are summarized in Table 1. Altogether, 88 parameters are optimized by the genetic algorithm. Five of these parameters pertain to cell geometry, namely, the anode thickness L_n , separator thickness L_s , cathode thickness L_p , anode particle radius R_n , and cathode particle radius R_p . One may directly measure these quantities by disassembling the cell. However, our aim is to use non-destructive methods for identifying the parameters. Three parameters characterize ion diffusion rates. They include the solid diffusivity d_{1n} in the anode, solid diffusivity d_{1p} in the cathode, and solution diffusivity d_2 . One parameter governs the fraction of the intercalation current carried by Li-ions, namely, the transference number t^+ . Two parameters govern rate kinetics, namely, the k -rates k_n in the anode and k_p in the cathode. These multiplicatively affect the current densities generated by the electrochemical reactions. One parameter scales the solution conductivity and diffusivity to their effective values, namely, the Brugman number b . Three parameters summarize the cell's porosity, namely, the solution volume fractions ε_{2n} for the anode, ε_{2s} for the separator and ε_{2p} for the cathode. One parameter captures the effective impedance of the anode-side solid electrolyte interphase layer, namely, R_{SEI} . The last scalar parameter is the initial concentration of the solution, c_2 , which we assume to be uniformly constant in space. This variable reflects the amount by which the battery electrolyte is initially lithiated.

In addition to the above 17 scalar parameters, the GA also optimizes three parametric functions in the DFN model. Two of these functions are the equilibrium potential functions, u_{nref} and u_{pref} , of the anode and cathode, respectively. We parameterize these functions using 33 control points each, and use monotonic splines to interpolate between these points [30]. The third function is $\kappa^{\text{eff}}(c_2)$, which determines the effective conductivity of the solution as a function of solution concentration. We parameterize this function using five control points spaced linearly from 0 mol m^{−3} to

4000 mol m⁻³, and interpolate between these control points using conventional cubic splines with natural end conditions [31].

Several constraints are placed on the above parameters in the genetic algorithm. All of these constraints are related to underlying identifiability issues within the model – each of them improves parameter identifiability by first removing parameters from the optimization problem and then algebraically relating them to parameters remaining within the optimization problem. First, we constrain the capacity of each electrode to equal exactly 2.7 Ah. This constraint provides two key benefits. It creates two 0.2 A-h buffers in each electrode, which improves the numerical stability of the DFN model. These buffers add 0.2 A-h of capacity to the maximum and minimum values of the electrodes. This allows the GA to tolerate minor local over and under filling of electrodes as it searches for the correct parameter values. Finally, it eliminates the interplay between changes in electrode charge capacity and changes in equilibrium potential functions versus capacity. The second optimization constraint forces the three electrode widths (L_n , L_s , L_p) and the area of the sheet rolled up inside the battery to collectively fit within the volume of the battery cell. Constraining the sheet area is particularly important because it acts as a multiplicative scale factor relating applied current to internal current density. The third constraint sets the volume fractions ε_1 and ε_2 in the anode and cathode to sum to exactly one. The final constraint sets the solid conductivities σ_{1n} and σ_{1p} to equal 100, consistent with [20]. This is justified since both conductivities have absolutely zero effect on the voltage trajectory (so long as they are both positive). Not all of these constraints are fully physically justified: a fact that reflects the presence of underlying identifiability issues. This motivates the Fisher information study in Section 7.

5. Parameter optimization scheme

To identify the DFN model's parameters, we first choose: (i) an optimization objective representing the model's accuracy, and (ii) experimental data sets for which this metric is optimized. The parameter identification objective we use in this paper is to minimize the L^2 error between the experimentally measured voltage $V(t)$ and DFN-simulated voltage trajectories $\hat{V}(t; \bar{\theta})$, for a given battery current trajectory, with respect to the DFN model parameter vector $\bar{\theta}$, i.e.,

$$\min_{\bar{\theta}} \int_0^T (V(t) - \hat{V}(t; \bar{\theta}))^2 dt \quad (9)$$

We optimize the above objective using only two of the seven cycles previously mentioned, *Chirp* and *Naturalistic1*, leaving the remaining 5 cycles for model validation. The *Chirp* cycle makes SoC-dependent and rate-dependent parameters easier to identify by sweeping through the full range of battery states of charge at different charge/discharge rates. Furthermore, the *Naturalistic1* cycle makes parameters associated with battery transients easier to identify due to rich frequency content resulting from PHEV drive cycle dynamics.

The genetic algorithm optimizes the above L^2 error over the course of the *Chirp* and *Naturalistic1* cycles by varying 88 of the DFN model's parameters. Genetic algorithms are well-suited for such large-scale optimization, especially when gradient information is difficult to obtain analytically or numerically. Fig. 4 provides a high-level snapshot of this article's GA-based DFN parameter identification scheme. The optimization process starts with the selection of inputs to the DFN model, in this case the *Chirp* and *Naturalistic1* current profiles versus time. We apply these current profiles experimentally to the battery, and measure the resulting voltage output. Next, we initialize the GA to a randomized population, where each population member is a DFN model parameter

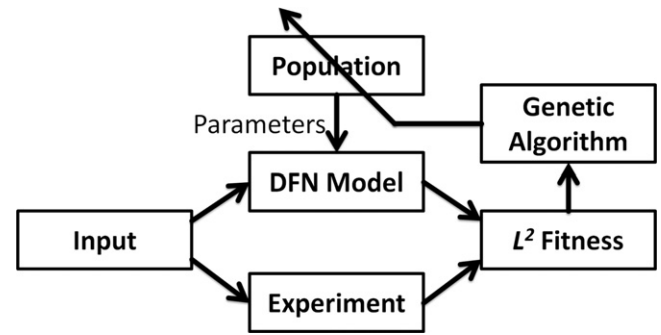


Fig. 4. Optimizing model parameters via a genetic algorithm.

set. The DFN model is simulated for each population member, and a comparison of the resulting simulated voltage versus experimental data furnishes a “fitness” value based on the inverse of the L^2 voltage fitting error. Population members are selected for removal at random by a fitness-weighted roulette game. This selection process is elitist, in the sense that the fittest population member is excluded from removal. Once the fitness-based selection is complete, we use binary mutation and crossover operators to create new population members. Parents are chosen randomly for mutation, with a selection probability weighted by their fitness. Mutations occur in a purely random manner, and are not weighted by fitness. The DFN model is then used once more to assign fitness values to the new population members, and the process repeats until convergence to a minimal model fitting error level. The final parameter values are obtained from the fittest member of the population. For further background on GA-based optimization, the reader is referred to [32].

To ensure the convergence of the GA an additional optimization was conducted (henceforth we will refer to this as the “tuning” optimization and the first optimization as the “base” optimization). The tuning optimization started with a population centered about the base optimization’s fittest population member. Additionally only parameters that were in the identifiable set were taken as variables in this optimization. Recall that to determine this set one needs to already be close to the optimum as the identifiable set is based on local identifiability properties (which is why it could not be computed a priori for the base optimization). The tuning optimization converged and slightly improved on the base optimization’s result.

The base (tuning) optimization process occurs in the R^{88} (R^{43}) Euclidean space, with each parameter quantized at 16 bits. This is a very large optimization space, comprising 7.083×10^{423} (1.284×10^{207}) possible parameter sets. We employ two main tools to render these optimizations numerically tractable. First, we use model reduction to accelerate the speed with which the DFN model is simulated, with minimal loss of accuracy. Specifically, we use a Legendre modal coordinate expansion similar to [14], together with algebraic constraint quasi-linearization similar to [8], to improve the DFN model’s simulation speed. We apply quasi-linearization directly to the Legendre modal coordinates, allowing for efficient solution of the algebraic constraints imposed by the coupled ϕ_1 and ϕ_2 boundary values problems. This improves computational speed to the point where we are able to simulate the DFN model for each new set of parameters in up to 63 s of computation time. Second, we parallelize the GA at the level of simulation function calls, with one server program coordinating multiple quad-core computers, which is a typical Master-Slave arrangement. Custom Java computer code handles Master-Slave information exchange over a TCP/IP network within a MATLAB implementation of the GA and DFN model. Altogether, this use of model reduction in conjunction with parallel processing makes it possible for five quad-core

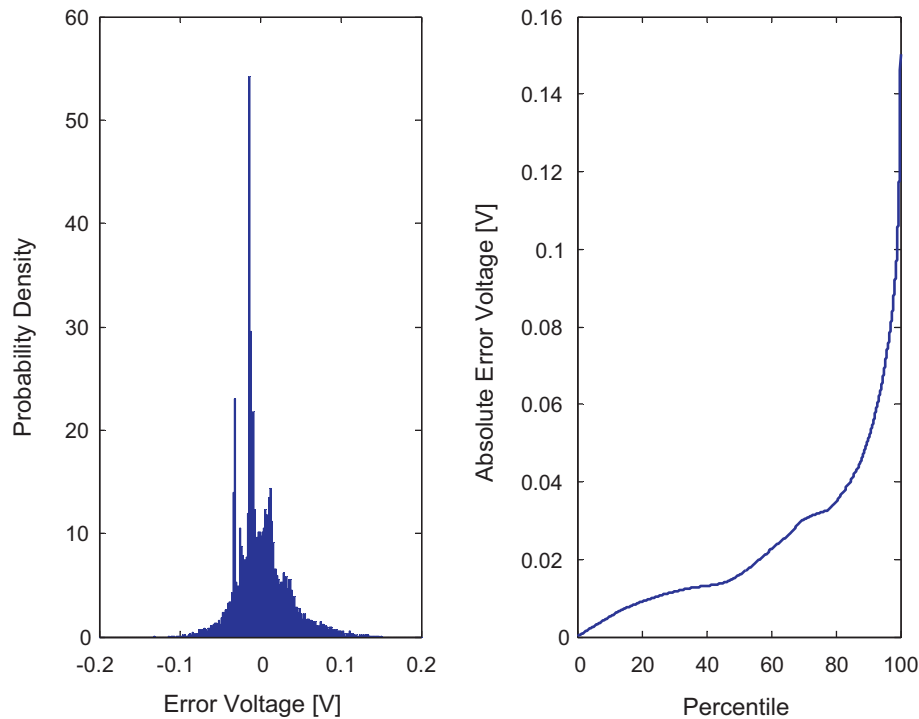


Fig. 5. Probability density plot of voltage error and the percentiles of absolute voltage error for all five of the validation cycles.

computers (Intel Q8200) to complete the optimization in approximately three weeks.

6. Validation results

One of the major results of this paper is a set of GA-fitted parameter values that match all five validation cycles; see Fig. 5 and Table 2. These parameters are based on the tuning optimization which offers slight improvements over a related set of values identified previously [8], which have already been used in two studies of PHEVs: one on power management and one on charge pattern optimization [33,34]. The values of the fitted parameters are given in Tables 3 and 4. Additional parameters necessary to run the DFN model but not explicitly optimized are listed in Table 5. These parameters are implicitly related to the optimization process, in the sense that they are functions of the optimally identified parameters; see Section 5 for details. Relative error in voltage and – consequently – power never exceeds 5% for any of the validation cycles. As shown in Table 2, the 50th percentile of voltage error is 15.8 mV and the 90th percentile of voltage error is still only 50.5 mV.

To examine the accuracy of the optimal parameter fit further, consider the results for the *Naturalistic2* and *LA92x2* validation cycles, which are representative of the set of five cycles. *Naturalistic2* is based on recorded data from a real driver's evening commute, as opposed to *Naturalistic1*, which is used for fitting and

represents a morning commute. Fig. 6 shows traces of voltage error and Fig. 7 shows traces of power error for *Naturalistic2*. The voltage error never exceeds 118.9 mV and the 50th percentile of voltage error is 12.5 mV. Fig. 8 presents a probability density plot and a percentile plot of this error.

The results for *LA92x2* are similar to those for *Naturalistic2*. Figs. 9 and 10 give the voltage and power trajectories along with their relative and absolute errors. Voltage error never exceeds 150.3 mV and the 50th percentile of voltage error is 28.0 mV. Fig. 11 presents probability density and percentile plots of this error.

As a final validation check, we examine whether the voltage errors for the five validation cycles are correlated with either input current or state of charge (SoC). Such correlation would suggest failure to accurately represent internal battery resistance or open-circuit potential as a function of SoC, respectively. Table 6 presents the R^2 correlation values between voltage error on the one hand and battery current and SoC on the other hand, for each of the validation cycles. None of the validation cycles have voltage errors linearly correlated with input current, which implies that the identified model captures at least internal battery resistance very well. The upper bound on the correlation between model error and SoC is $R^2 = 0.433$ which is the case for the *Naturalistic2* drive cycle. As a point of comparison the correlation between predicted and measured voltage for *Naturalistic2* is R^2 of 0.871, implying that the identified model captures the dependence of battery dynamics on SoC quite well. This SoC is the “system” SoC (as opposed to the “chemical” SoC which would be calculated based on the quantity of Li in the anode) and is calculated for the battery by integrating and scaling current, knowing that each experiment was initialized at 90% SoC, i.e.,

$$\text{SoC}_{\text{System}} = \frac{\int_0^t I(\tau) d\tau}{\text{Name Plate Capacity}} + 0.9 \quad (10)$$

In summary, this section shows that the DFN model, together with the parameter values identified in this paper, accurately simulates battery cells under the loading characteristics of PHEVs. This

Table 2
Percentile errors of voltage [mV].

Drive cycle	Percentile of error [mV]			
	25%	50%	75%	100%
<i>Naturalistic2</i>	9.8	12.5	13.6	118.9
<i>LA92x2</i>	11.7	28.0	41.0	150.3
<i>US06x3</i>	10.6	23.4	41.5	140.0
<i>SC03x4</i>	9.7	21.0	32.7	146.3
<i>UDDSx2</i>	12.0	28.3	33.2	140.9
All val cycles	10.4	15.8	31.9	150.3

Table 3
First half of optimized parameters.

Name	Value	Unit	Variance	95% Confidence interval		
				Min	Max	Rel%
L_n	2.880E–05	m	1.30E–15	2.87E–05	2.89E–05	0.25%
L_s	1.697E–05	m	U	U	U	U
L_p	6.508E–05	m	3.45E–14	6.47E–05	6.54E–05	0.57%
R_n	3.600E–06	m	2.98E–18	3.60E–06	3.60E–06	0.10%
R_p	1.637E–07	m	U	U	U	U
t^*	2.495E–01	–	U	U	U	U
b	1.439E+00	–	1.11E–02	1.23E+00	1.65E+00	14.63%
d_2	6.930E–10	m ² s ^{–1}	9.55E–19	–1.26E–09	2.65E–09	281.98%
ε_{2n}	6.188E–01	–	2.62E–02	2.95E–01	9.43E–01	52.33%
ε_{2s}	3.041E–01	–	U	U	U	U
ε_{2p}	5.206E–01	–	4.49E–03	3.87E–01	6.55E–01	25.73%
d_{1n}	8.275E–14	m ² s ^{–1}	1.44E–26	–1.57E–13	3.23E–13	289.99%
d_{1p}	1.736E–14	m ² s ^{–1}	U	U	U	U
k_n	8.692E–07	(A m ^{–2}) (mol m ^{–3}) ^{1+α}	6.38E–20	8.69E–07	8.70E–07	0.06%
k_p	1.127E–07	(A m ^{–2}) (mol m ^{–3}) ^{1+α}	U	U	U	U
R_{SEI}	3.697E–03	Ω m ²	6.49E–10	3.65E–03	3.75E–03	1.38%
c_2	1.040E+03	mol m ^{–3}	8.42E+00	1.03E+03	1.05E+03	0.56%
u_{nref1}	3.959E+00	V	U	U	U	U
u_{nref2}	3.400E+00	V	U	U	U	U
u_{nref3}	1.874E+00	V	U	U	U	U
u_{nref4}	9.233E–01	V	5.15E–02	4.70E–01	1.38E+00	49.14%
u_{nref5}	9.074E–01	V	2.54E–05	8.97E–01	9.17E–01	1.11%
u_{nref6}	6.693E–01	V	3.27E–04	6.33E–01	7.06E–01	5.40%
u_{nref7}	2.481E–03	V	U	U	U	U
u_{nref8}	1.050E–03	V	U	U	U	U
u_{nref9}	1.025E–03	V	U	U	U	U
u_{nref10}	8.051E–04	V	U	U	U	U
u_{nref11}	5.813E–04	V	U	U	U	U
u_{nref12}	2.567E–04	V	U	U	U	U
u_{nref13}	2.196E–04	V	U	U	U	U
u_{nref14}	1.104E–04	V	U	U	U	U
u_{nref15}	3.133E–06	V	U	U	U	U
u_{nref16}	1.662E–06	V	U	U	U	U
u_{nref17}	9.867E–07	V	U	U	U	U
u_{nref18}	3.307E–07	V	U	U	U	U
u_{nref19}	1.570E–07	V	U	U	U	U
u_{nref20}	9.715E–08	V	U	U	U	U
u_{nref21}	5.274E–09	V	U	U	U	U
u_{nref22}	2.459E–09	V	U	U	U	U
u_{nref23}	7.563E–11	V	U	U	U	U
u_{nref24}	2.165E–12	V	U	U	U	U
u_{nref25}	1.609E–12	V	U	U	U	U
u_{nref26}	1.594E–12	V	U	U	U	U
u_{nref27}	1.109E–12	V	U	U	U	U

GA optimized parameter values for the DFN model. Variances are computed using Fisher information. U indicates an unidentifiable parameter.

accuracy is evident from the small errors in the voltage – and consequently, power – traces of the DFN model compared to experimental data. The parameter values in this paper make it possible to accurately simulate the ANR26650M1A cell for PHEV applications.

7. Fisher information and parameter variance

Section 6 of this article assesses the degree to which the identified DFN model is able to replicate input–output voltage/current battery cycling behavior. The overarching goal of this section, in contrast, is to evaluate the quality of the model parameter estimates. Previous work by the authors pursues this goal using the identifiability matrix, and shows that while the identified DFN model fits input–output voltage/current data very well, certain model parameters are unidentifiable [8]. This article enhances this analysis by quantifying the parameter estimation variance via Fisher information techniques. Fisher information provides the minimum variance for parameter estimation via the Cramér–Rao inequality [9,10]. The Cramér–Rao inequality applies to the GA algorithm used herein since we use this algorithm as a maximum

likelihood estimator (the GA chooses parameters values to minimize L^2). Thus the inverse of the Fisher information matrix is the covariance of estimating the model parameters. Since there is only one output, Fisher information can be calculated by multiplying the identifiability matrix by the voltage sensor's variance. This variance was computed from the voltage error between simulation and experiment for the fitting data sets.

The variance of the estimated parameters is presented in Tables 3 and 4 along with 95% (two standard deviations) confidence bounds and relative error. For each parameter, this relative error is the upper 95% confidence bound minus the parameter's estimated value, divided by this estimated value. Not all of the parameters are identifiable, and those that are unidentifiable are marked with a 'U'. Unidentifiability was determined using the method in [8] where the minimum condition number for the identifiability matrix was taken as 10^{-10} . Lower condition numbers caused unreasonable numerical errors in the inversion of the Fisher information matrix.

The process of partitioning a given parameter set into identifiable versus unidentifiable parameters makes it possible to make

Table 4
Second half of optimized parameters.

Name	Value	Unit	Variance	95% Confidence interval		
				Min	Max	Rel%
u_{nref28}	4.499E–13	V	U	U	U	U
u_{nref29}	2.250E–14	V	U	U	U	U
u_{nref30}	1.335E–14	V	U	U	U	U
u_{nref31}	1.019E–14	V	U	U	U	U
u_{nref32}	2.548E–16	V	U	U	U	U
u_{nref33}	1.654E–16	V	U	U	U	U
u_{pref1}	5.502E+00	V	U	U	U	U
u_{pref2}	4.353E+00	V	1.79E–02	4.09E+00	4.62E+00	6.15%
u_{pref3}	3.683E+00	V	1.36E–05	3.68E+00	3.69E+00	0.20%
u_{pref4}	3.554E+00	V	1.64E–06	3.55E+00	3.56E+00	0.07%
u_{pref5}	3.493E+00	V	9.58E–06	3.49E+00	3.50E+00	0.18%
u_{pref6}	3.400E+00	V	8.66E–06	3.39E+00	3.41E+00	0.17%
u_{pref7}	3.377E+00	V	8.03E–06	3.37E+00	3.38E+00	0.17%
u_{pref8}	3.364E+00	V	8.51E–06	3.36E+00	3.37E+00	0.17%
u_{pref9}	3.363E+00	V	1.28E–05	3.36E+00	3.37E+00	0.21%
u_{pref10}	3.326E+00	V	1.09E–05	3.32E+00	3.33E+00	0.20%
u_{pref11}	3.324E+00	V	1.27E–05	3.32E+00	3.33E+00	0.21%
u_{pref12}	3.322E+00	V	1.13E–05	3.32E+00	3.33E+00	0.20%
u_{pref13}	3.321E+00	V	1.57E–05	3.31E+00	3.33E+00	0.24%
u_{pref14}	3.316E+00	V	1.54E–05	3.31E+00	3.32E+00	0.24%
u_{pref15}	3.313E+00	V	1.40E–05	3.31E+00	3.32E+00	0.23%
u_{pref16}	3.304E+00	V	1.64E–05	3.30E+00	3.31E+00	0.25%
u_{pref17}	3.295E+00	V	1.20E–05	3.29E+00	3.30E+00	0.21%
u_{pref18}	3.293E+00	V	6.76E–06	3.29E+00	3.30E+00	0.16%
u_{pref19}	3.290E+00	V	1.11E–05	3.28E+00	3.30E+00	0.20%
u_{pref20}	3.279E+00	V	1.22E–05	3.27E+00	3.29E+00	0.21%
u_{pref21}	3.264E+00	V	1.19E–05	3.26E+00	3.27E+00	0.21%
u_{pref22}	3.261E+00	V	1.04E–05	3.25E+00	3.27E+00	0.20%
u_{pref23}	3.253E+00	V	6.13E–06	3.25E+00	3.26E+00	0.15%
u_{pref24}	3.245E+00	V	7.85E–06	3.24E+00	3.25E+00	0.17%
u_{pref25}	3.238E+00	V	1.59E–05	3.23E+00	3.25E+00	0.25%
u_{pref26}	3.225E+00	V	1.09E–05	3.22E+00	3.23E+00	0.20%
u_{pref27}	3.207E+00	V	5.81E–05	3.19E+00	3.22E+00	0.48%
u_{pref28}	2.937E+00	V	1.64E–04	2.91E+00	2.96E+00	0.87%
u_{pref29}	2.855E+00	V	1.09E–04	2.83E+00	2.88E+00	0.73%
u_{pref30}	2.852E+00	V	1.13E–04	2.83E+00	2.87E+00	0.74%
u_{pref31}	1.026E+00	V	U	U	U	U
u_{pref32}	–1.120E+00	V	U	U	U	U
u_{pref33}	–1.742E+00	V	U	U	U	U
$\kappa 1$	1.050E–01	$\Omega^{-1} \text{ m}^{-1}$	U	U	U	U
$\kappa 2$	1.760E–01	$\Omega^{-1} \text{ m}^{-1}$	U	U	U	U
$\kappa 3$	2.190E–01	$\Omega^{-1} \text{ m}^{-1}$	U	U	U	U
$\kappa 4$	8.166E–02	$\Omega^{-1} \text{ m}^{-1}$	U	U	U	U
$\kappa 5$	3.014E–02	$\Omega^{-1} \text{ m}^{-1}$	U	U	U	U

GA optimized parameter values for the DFN model. Variances are computed using Fisher information. U indicates an unidentifiable parameters.

quantitative statements regarding these parameters' accuracy. Unidentifiable parameters cannot be estimated from experimental measurements. One can only, therefore, estimate their accuracy by comparing their estimated values with the published literature. Identifiable parameters can, in contrast, be estimated

from experimental data. Furthermore, the accuracy of these identifiable parameters can itself be methodically estimated from the Fisher information matrix, provided one can associate a priori assumed levels of error with the unidentifiable parameters. The remainder of this article demonstrates the process of methodically calculating the estimation errors associated with the identifiable parameters, under the optimistic assumption that the unidentifiable parameters are known a priori. Our goal, here, is to demonstrate the value of identifiability analysis for the DFN model, rather than to quantify DFN parameter estimation errors exactly. It is very important to note, here, that the choice of which parameters

Table 5
Parameters not directly involved in GA.

Name	Value	Unit
c_{1n}	2.479E+04	mol m^{-3}
c_{1p}	1.649E+03	mol m^{-3}
c_{1nmax}	2.948E+04	mol m^{-3}
c_{1pmax}	1.035E+04	mol m^{-3}
T	2.982E+02	K
α	5.000E–01	–
ε_{1n}	3.812E–01	–
ε_{1p}	4.794E–01	–
σ_n	1.000E+02	$\text{m}^{-1} \Omega^{-1}$
σ_p	1.000E+02	$\text{m}^{-1} \Omega^{-1}$
$Area$	3.108E–01	m^2

Note: all of these parameters are either fixed or algebraically related to the optimization variables.

Table 6
 R^2 coefficients of correlation with voltage estimation error.

Drive cycle	I_{app}	SoC
<i>Naturalistic2</i>	0.023	0.433
<i>LA92x2</i>	0.127	0.190
<i>US06x3</i>	0.153	0.151
<i>SC03x4</i>	0.179	0.204
<i>UDDSx2</i>	0.100	0.246

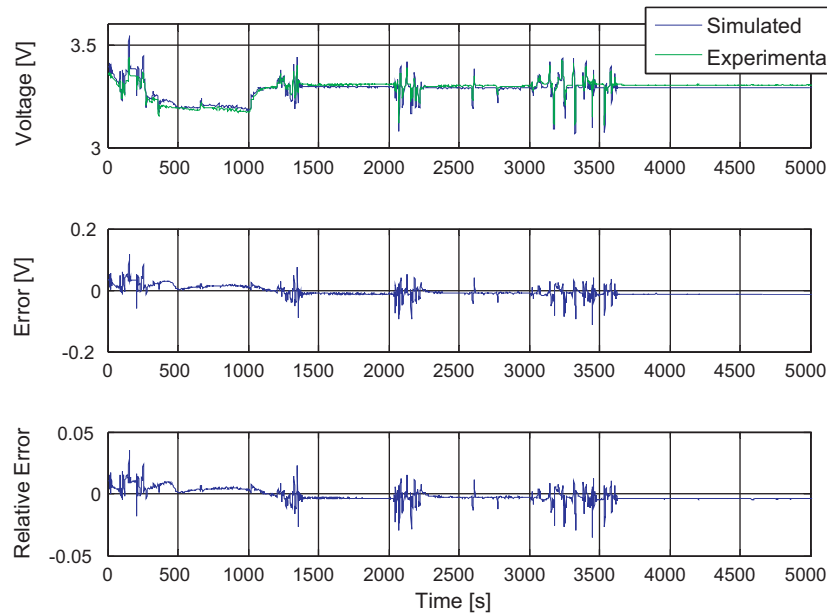


Fig. 6. Voltage response for *Naturalistic2*.

are identifiable versus unidentifiable has a significant impact on the identification errors computed by this process. One must therefore be very vigilant when making this choice/partitioning.

Of the eleven identifiable scalar parameters six are estimated with good accuracy (relative error <2%). These are associated with geometry: L_n the anode width, L_p the cathode width, R_n the spherical radius in the anode, k_n the k -rate in the anode, R_{SEI} the solid electrolyte interface resistance, and c_2 the initial concentration of Li in solution. The remaining five scalar parameters all have relative errors greater than 25%. It is important to note that these variances correspond to the case where one attempts to identify all model parameters simultaneously, with the unidentifiable values fixed. If one knows some parameters with certainty and can therefore estimate a smaller subset of the DFN model parameters, the

variance in these parameters will be lower (or at least the same). For example, if one is designing a state of health estimator whose sole goal is to estimate R_{SEI} assuming all other DFN model parameters to be known, the variance in estimation would be $4.387\text{E}-014$, and the relative error in estimating R_{SEI} would decrease from 1.38% to 0.0113%. These results are important, because they: (i) quantify the errors in the parameters identified herein, (ii) highlight the difficulties in estimating specific parameters solely through voltage and current time traces, and (iii) underscore the importance of examining the identifiability of all DFN model parameters, not just a subset of those parameters.

To provide further insights into the DFN model's parameter identifiability, Figs. 12 and 13 present the estimates of the cathode- and anode-side equilibrium potentials versus SoC, along with their

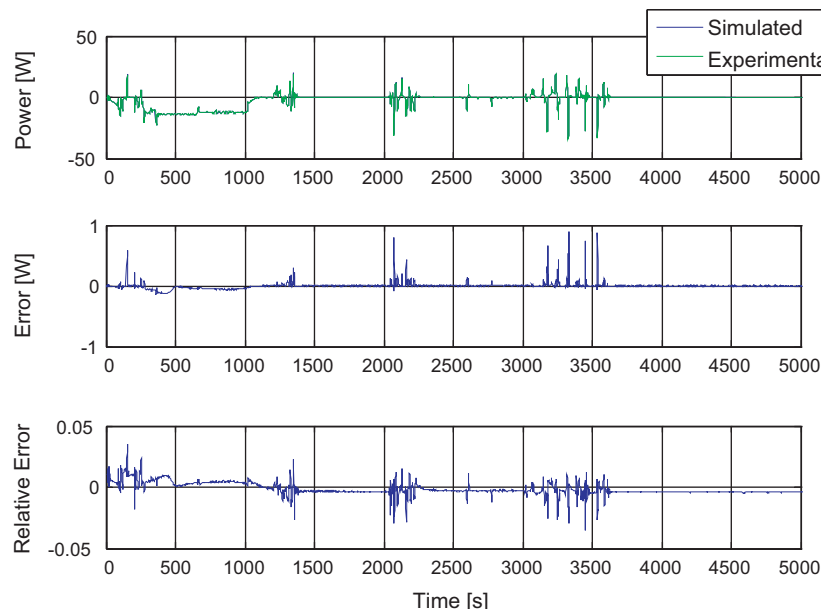


Fig. 7. Power response for *Naturalistic2*.

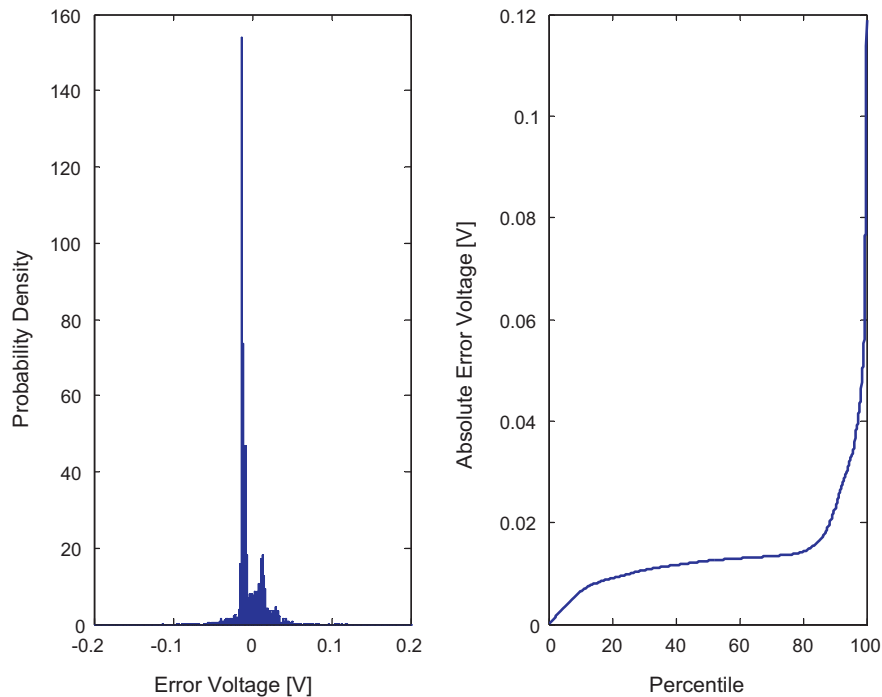


Fig. 8. Probability density plot of voltage error and the percentiles of absolute voltage error for *Naturalistic2*.

95% confidence bounds. For plotting purposes, the unidentifiable parameters have confidence bounds at $-\infty$ and ∞ . In the model these equilibrium potential functions are represented by monotonic cubic splines in terms of SoC. Here we plot these functions as piecewise linear since the confidence bounds are only for the control points. Between the two equilibrium potential functions, u_{pref} has much less variance than u_{nref} . Specifically, the estimation of u_{pref} exhibits low variance, where the confidence bounds correspond to relative errors less than 1% for 0% SoC to 95% SoC (where this SoC does not include the buffers). In contrast, most of u_{nref} is unidentifiable, and even the identifiable control points still have very high variances. The equilibrium potential functions provide

a good example of the effects of assuming that the unidentifiable values are correct. Since u_{pref} is very dependent on u_{nref} , and u_{nref} is largely incorrect, u_{pref} is mostly identifiable – but to make the u_{pref} values accurate one needs to plug in accurate values for the u_{nref} first. The conductivity function $\kappa_2^{eff}(c_2)$ is completely unidentifiable – indicating that the interplay between solution concentration and conductivity could not be determined through these experiments.

Parameter identifiability and variance in estimation are the function of several important factors. First, they are a function of which parameters are being identified and which are already assumed known. This leads to cases where parameter

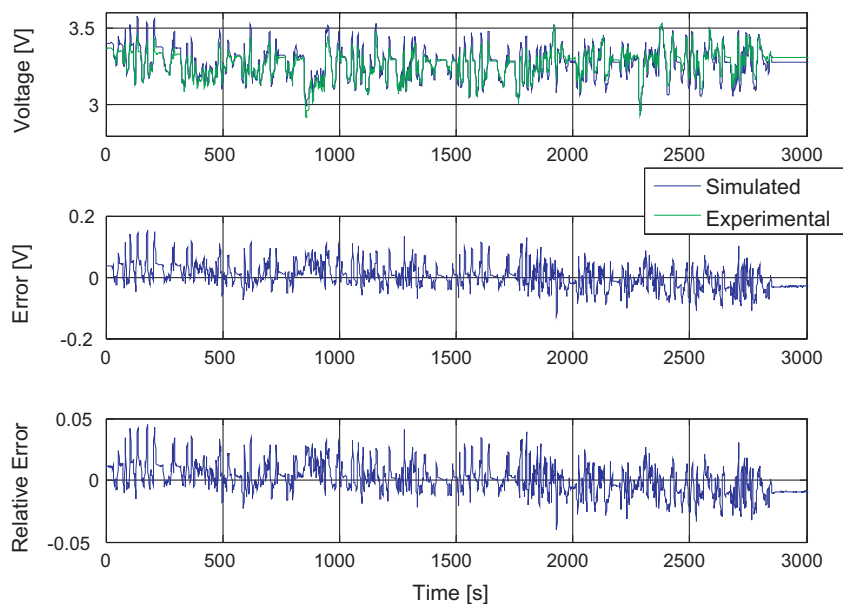


Fig. 9. Voltage response for *LA92x2*.

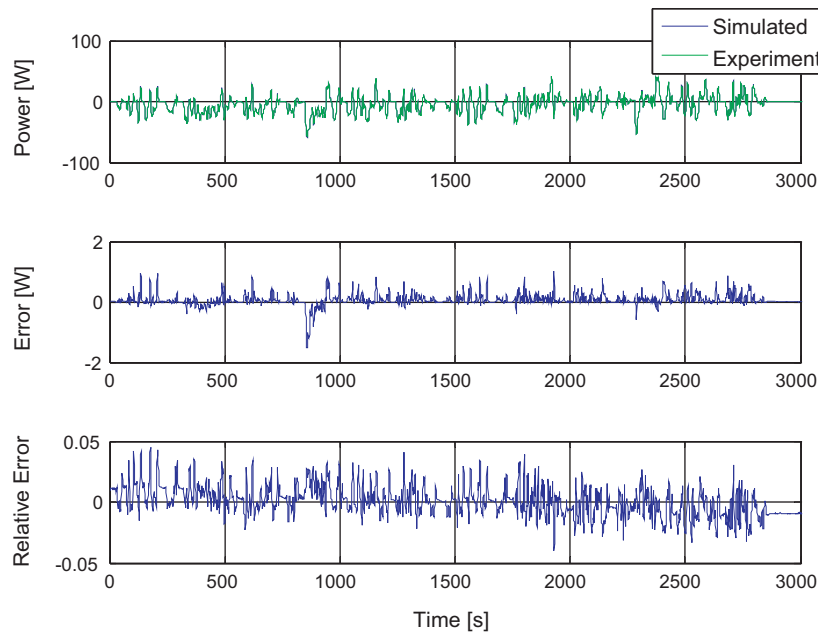


Fig. 10. Power response for LA92x2.

estimation errors can be improved dramatically by changing the number of known parameters versus unknown ones (as shown previously in the case of R_{SEI}). Parameter identifiability also depends on the values of the parameters after they have been fit to the data. This is due to Fisher information being a local quantity in the parameter space. In general, this makes it impossible to determine which parameters will be identifiable a priori. Finally we note that the experiments themselves can greatly affect parameter identifiability. Both the structure of the battery experiment (including placement of sensors and actuators) and the

experiment's trajectory can affect parameter identifiability. As an example of structure, if our cell had a third electrode then we would have been able to measure two voltages – likely improving our ability to identify u_{nref} and u_{pref} simultaneously. As an example of the experimental trajectory's impact, the *Natuarlistic2* and *Chirp* cycles are different in terms of the battery dynamics they excite, and therefore different in their impact on parameter identifiability. All of these factors underscore that matching input–output data is not enough to guarantee that the model parameter values are physically accurate.

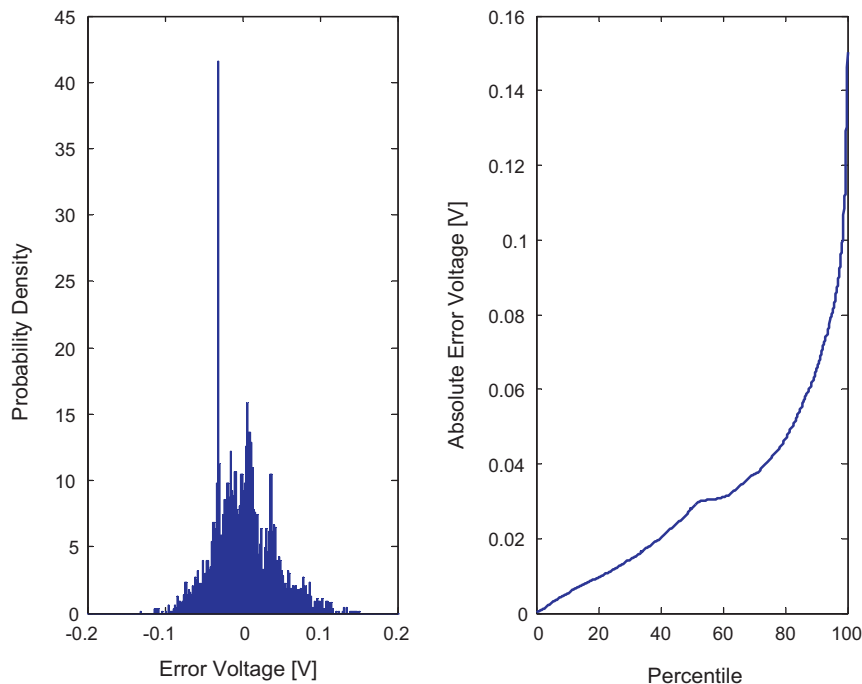


Fig. 11. Probability density plot of voltage error and the percentiles of absolute voltage error for LA92x2.

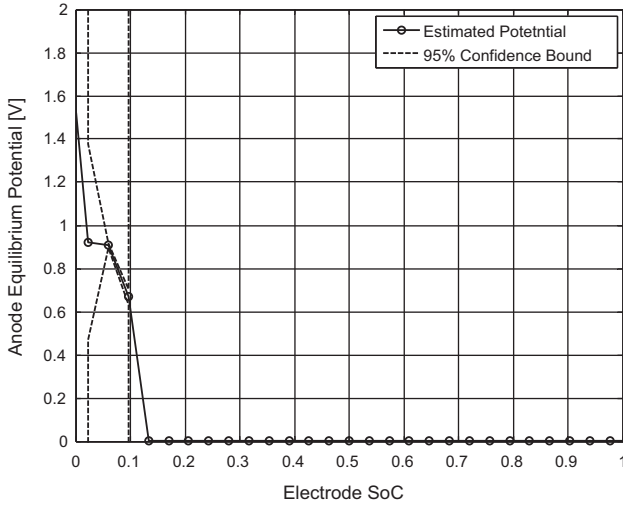


Fig. 12. Estimated anode equilibrium potential u_{nref} with 95% confidence bounds.

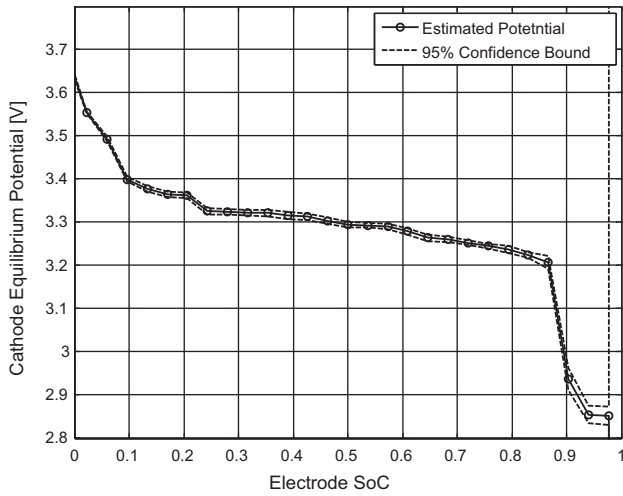


Fig. 13. Estimated cathode equilibrium potential u_{pref} with 95% confidence bounds.

8. Summary and conclusion

This article uses a genetic algorithm to match the Doyle–Fuller–Newman battery model's voltage predictions to experimental measurements, for given input current profiles. We optimize 88 parameters of the DFN model, including parameterizations of the anode and cathode equilibrium potential functions and the solution conductivity function. The end result is a set of parameter values for the DFN model that predicts cell voltage and power with 5% relative error for all of the validation data sets examined in this work. All of these validation data sets are based on simulated plug-in hybrid electric vehicle battery pack currents that exhibit high charge/discharge rates and are highly transient in nature. For all of the validation cycles aggregated together, the 50th percentile of voltage error 15.8 mV, and the 90th percentile of voltage error is still only 50.5 mV. This high level of accuracy justifies the use of the DFN model for the lithium-iron-phosphate (LiFePO₄) cathode chemistry examined in this work. In fact, the parameter values identified herein have already been used in two studies involving PHEVs [33,34]. Additionally, this paper presents some of the computational logistics involved in using a GA for parameter identification.

The identification procedure used herein makes it possible to find a set of parameter values for the DFN model noninvasively. Unfortunately, this noninvasiveness causes some parameters to be unidentifiable or have a large estimation uncertainty. While this does not affect the accuracy of the model response, it does mean that one must be careful when using these parameters in other contexts.

Acknowledgments

This work was supported by the National Science Foundation EFRI-RESIN Grant 0835995, and the Michigan Public Service Commission.

Appendix A. Boundary conditions

This appendix summarizes the boundary conditions present in the DFN model. The effective values of various quantities are related to the volume fraction and the Bruggeman number as follows:

$$d_{2eff} = d_2 \varepsilon_{2j}^b \quad \forall j \in \{n, s, p\} \quad (A.1)$$

$$\sigma_{jef} = \sigma \varepsilon_{1j} \quad \forall j \in \{n, p\} \quad (A.2)$$

$$\kappa_{eff}(c_2) = \kappa(c_2) \varepsilon_{2j}^b \quad \forall j \in \{n, s, p\} \quad (A.3)$$

$$\kappa_D(c_2) = \kappa_{eff}(c_2) \left(\frac{2RT(1-t^+)}{F} \right) \quad (A.4)$$

For solid concentration c_1 :

$$\frac{\partial}{\partial r} c_1(r) = 0, \quad @r = 0 \quad (A.5)$$

$$\frac{\partial}{\partial r} c_1(r) = -\frac{J_j(r)}{d_{1j} a_j F}, \quad @r = R, \quad \forall j \in \{n, p\} \quad (A.6)$$

For solution concentration c_2 :

$$\frac{\partial}{\partial x} c_2(x) = 0 \quad @x = 0, \quad x = L_n + L_s + L_p \quad (A.7)$$

$$d_{2eff} \Big|_{anode} \frac{\partial}{\partial x} c_2(x) = d_{2eff} \Big|_{separator} \frac{\partial}{\partial x} c_2(x) \quad @x = L_n \quad (A.8)$$

$$d_{2eff} \Big|_{separator} \frac{\partial}{\partial x} c_2(x) = d_{2eff} \Big|_{cathode} \frac{\partial}{\partial x} c_2(x) \quad @x = L_n + L_s \quad (A.9)$$

In addition c_2 is equated at the anode/separator interface and the separator/cathode interface.

For solid potential ϕ_1 :

$$\frac{\partial}{\partial x} \phi_1(x) = 0 \quad @x = L_n, \quad x = L_n + L_s \quad (A.10)$$

$$\phi_1(x) = 0 \quad @x = 0 \quad (A.11)$$

This places the ground at the negative electrode. At the positive electrode one can choose between a current and voltage input. For the current input:

$$\frac{\partial}{\partial x} \phi_1(x) = \frac{i_{app}}{Area \times \sigma_{neff}} \quad @x = L_n + L_s + L_p \quad (A.12)$$

where *Area* converts from current density to absolute current.

For the voltage input:

$$\phi_1(x) = Volt_{applied} \quad @x = L_n + L_s + L_p \quad (A.13)$$

For the solution potential ϕ_2 :

$$\frac{\partial}{\partial x} \phi_2(x) = 0 \quad @x = 0, \quad x = L_n + L_s + L_p \quad (A.14)$$

$$\begin{aligned} \kappa_{eff}(c_2) \Big|_{anode} \frac{\partial}{\partial x} \phi_2(x) + \kappa_D(c_2) \Big|_{anode} \frac{\partial}{\partial x} \ln(c_2(x)) \\ = \kappa_{eff}(c_2) \Big|_{separator} \frac{\partial}{\partial x} \phi_2(x) + \kappa_D(c_2) \Big|_{separator} \frac{\partial}{\partial x} \ln(c_2(x)) \quad @x = L_n \end{aligned} \quad (A.15)$$

$$\begin{aligned} \kappa_{eff}(c_2) \Big|_{separator} \frac{\partial}{\partial x} \phi_2(x) + \kappa_D(c_2) \Big|_{separator} \frac{\partial}{\partial x} \ln(c_2(x)) \\ = \kappa_{eff}(c_2) \Big|_{cathode} \frac{\partial}{\partial x} \phi_2(x) + \kappa_D(c_2) \Big|_{cathode} \frac{\partial}{\partial x} \ln(c_2(x)) \quad @x \\ = L_n + L_s \end{aligned} \quad (A.16)$$

In addition ϕ_2 is equated at the anode/separator interface and the separator/cathode interface.

References

- [1] M. Doyle, T. Fuller, J. Newman, Modeling of galvanostatic charge and discharge of the lithium/polymer/insertion cell, *Journal of the Electrochemical Society* 140 (June) (1993) 1526–1533.
- [2] T. Fuller, M. Doyle, J. Newman, Simulation and optimization of the dual lithium ion insertion cell, *Journal of the Electrochemical Society* 141 (January) (1994) 1–10.
- [3] A. Elgowainy, A. Burnham, M. Wang, J. Molburg, A. Rousseau, Well-to-Wheels Energy Use and Greenhouse Gas Emissions Analysis of Plug-in Hybrid Electric Vehicles, Center for Transportation Research, Argonne National Laboratory, 2009.
- [4] S. Santhanagopalan, Q. Guo, R. White, Parameter estimation and model discrimination for a lithium-ion cell, *Journal of the Electrochemical Society* 154 (March) (2007) A198–A206.
- [5] C. Speltino, D. Domenico, G. Fiengo, A. Stefanopoulou, On the experimental identification of an electrochemical model of a lithium-ion battery: part II, in: *The European Control Conference*, Budapest, 2009.
- [6] A. Schmidt, M. Bitzer, A. Imre, L. Guzzella, Experiment-driven electrochemical modeling and systematic parameterization for a lithium-ion cell, *Journal of Power Sources* 195 (August) (2010) 5071–5080.
- [7] Y. Hu, S. Yurkovich, Y. Guezennec, B. Yurkovich, A technique for dynamic battery model identification in automotive applications using linear parameter varying structures, *Journal of Control Engineering Practice* 17 (October) (2009) 1190–1201.
- [8] J. Forman, S. Moura, J. Stein, H. Fathy, Genetic parameter identification of the Doyle–Fuller–Newman model from experimental cycling of a LiFePO₄ battery, in: *American Controls Conference*, San Francisco, 2011.
- [9] T. Cover, J. Thomas, *Elements of Information Theory*, John Wiley & Sons, New York, NY, 1991 (Chapter 12).
- [10] T. McWhorter, L.L. Scharf, Cramér–Rao bounds for deterministic modal analysis, *IEEE Transactions on Signal Processing* 41 (5) (1993) 1847–1866.
- [11] H. Wynn, N. Parkin, Sensitivity analysis and identifiability for differential equation models, in: *Conference on Decision and Control*, Orlando, 2001.
- [12] H. Khalil, *Nonlinear Systems*, Prentice Hall, Upper Saddle River, NJ, 2002 (Chapter 3).
- [13] J. Jacquez, T. Perry, Parameter estimation: local identifiability of parameters, *AJP – Endocrinology and Metabolism* 258 (1990) E727–E736.
- [14] V.R. Subramanian, V. Boovaragavan, V. Ramadesigan, M. Arabandi, Mathematical model reformulation for lithium-ion battery simulations: galvanostatic boundary conditions, *Journal of Electrochemistry* 156 (2009) A260–A271.
- [15] J.C. Forman, S. Bashash, J. Stein, H. Fathy, Reduction of an electrochemistry-based Li-ion battery model via quasi-linearization and Padé approximation, *Journal of the Electrochemical Society* 158 (2) (2011) A93–A101.
- [16] H. Fathy, Z. Filipi, J. Hagena, J. Stein, Review of hardware-in-the-loop simulation and its prospects in the automotive area, *The International Society for Optical Engineering* 6228 (2006) 1–20.
- [17] D. LeBlanc, J. Sayer, C. Winkler, R. Ervin, S. Bogard, J. Devonshire, M. Mefford, M. Hagan, Z. Bareket, R. Goodsell, et al., Road Departure Crash Warning System Field Operational Test: Methodology and Results, University of Michigan Transportation Research Institute, Tech. Rep. UMTRI-2006-9-1, June 2006.
- [18] M. Duoba, R. Carlson, F. Jehlik, J. Smart, S. White, Correlating dynamometer testing to in-use fleet results of plug-in hybrid electric vehicles, *World Electric Vehicle Journal* 3 (1) (2009).
- [19] S.J. Moura, H.K. Fathy, D.S. Callaway, J.L. Stein, A stochastic optimal control approach for power management in plug-in hybrid electric vehicles, *IEEE Transactions on Control Systems Technology* PP (March (99)) (2010) 1–11.
- [20] P. Ramadass, B. Haran, P. Gomadam, R. White, B. Popov, Development of first principles capacity fade model for Li-ion cells, *Journal of Electrochemistry* 151 (2004) A196–A203.
- [21] L. Laffont, C. Delacourt, P. Gibot, M. Yue Wu, P. Kooyman, C. Masquelier, J. Marie Tarascon, Study of the LiFePO₄/FePO₄ two-phase system by high-resolution electron energy loss spectroscopy, *Chemistry of Materials* 18 (November (23)) (2006) 5520–5529.
- [22] C. Delmas, M. Maccario, L. Croguennec, F. Le Cras, F. Weill, Lithium deintercalation in LiFePO₄ nanoparticles via a domino-cascade model, *Nature Materials* 23 (August (8)) (2008) 665–671.
- [23] G. Brunetti, D. Robert, P. Bayle-Guillemaud, J.L. Rouvière, E.F. Rauch, J.F. Martin, J.F. Colin, F. Bertin, C. Cayron, Confirmation of the domino-cascade model by LiFePO₄/FePO₄ precession electron diffraction, *Chemistry of Materials* 23 (October (20)) (2011) 4515–4524.
- [24] V. Srinivasan, J. Newman, Discharge model for the lithium iron-phosphate electrode, *Journal of the Electrochemical Society* 151 (October (10)) (2004) A1517–A1529.
- [25] V. Srinivasan, J. Newman, Existence of path-dependence in the LiFePO₄ electrode, *Journal of the Electrochemical Society* 9 (March (3)) (2006) A110–A114.
- [26] M. Safari, C. Delacourt, Mathematical modeling of lithium iron phosphate electrode: galvanostatic charge/discharge and path dependence, *Journal of the Electrochemical Society* 158 (February (2)) (2011) A63–A73.
- [27] M. Safari, C. Delacourt, Modeling of a commercial graphite/LiFePO₄ cell, *Journal of the Electrochemical Society* 158 (May (5)) (2011) A562–A571.
- [28] F. Liu, N. Siddique, P. Mukherjee, Nonequilibrium phase transformation and particle shape effect in LiFePO₄ material for Li-ion batteries, *Electrochemical and Solid-State Letters* 14 (10) (2011) A143–A147.
- [29] G. Singh, G. Ceder, M. Bazant, Intercalation dynamics in rechargeable battery materials: general theory and phase-transformation waves in LiFePO₄, *Electrochimica Acta* 53 (November (26)) (2008) 7599–7613.
- [30] F. Fritsch, R. Carlson, Monotone piecewise cubic interpolation, *SIAM Journal of Numerical Analysis* 17 (April) (1980) 238–246.
- [31] R. Burden, J. Faires, *Numerical Analysis*, 7th ed., Wadsworth, Pacific Grove, CA, 2001, pp. 146–147.
- [32] E. Cantú, *Paz Efficient and Accurate Parallel Genetic Algorithms*, Kluwer Academic Publishers, Norwell, MA, 2000 (Chapter 3).
- [33] S. Bashash, S.J. Moura, J.C. Forman, H.K. Fathy, Plug-in hybrid vehicle charge pattern optimization for energy cost and battery longevity, *Journal of Power Sources* 196 (January (1)) (2011) 541–549.
- [34] S.J. Moura, J.L. Stein, H.K. Fathy, Battery health conscious power management in plug-in hybrid electric vehicles via electrochemical modeling and stochastic control, *IEEE Transactions on Control Systems Technology*, in press, doi:10.1109/TCST.2012.2189773.